

55 Tesla coercive magnetic field in frustrated $\text{Sr}_3\text{NiIrO}_6$

John Singleton¹, Jae Wook Kim¹, Craig V. Topping^{1,2,3}, Anders Hansen¹, Eun-Deok Mun^{1,4}, Saman Ghannadzadeh³, Paul Goddard⁵, Xuan Luo^{6,7}, Yoon Seok Oh⁶, Sang-Wook Cheong⁶, Vivien S. Zapf¹

¹*National High Magnetic Field Laboratory (NHMFL), MS E536, Los Alamos National Laboratory, Los Alamos, NM 87545, USA*

²*Department of Chemistry, University of Edinburgh, Edinburgh, Midlothian EH8 9YL, United Kingdom*

³*University of Oxford, Department of Physics, The Clarendon Laboratory, Parks Road, Oxford, OX1 3PU, United Kingdom*

⁴*Department of Physics, Simon Fraser University, Burnaby, BC, V5A 1S6, Canada*

⁵*Department of Physics, University of Warwick, Gibbet Hill Road, Coventry, CV4 7AL, United Kingdom*

⁶*RCEM & Dept. of Physics and Astronomy, Rutgers University, Piscataway, NJ 08854, USA and*

⁷*POSTECH, Pohang University of Science and Technology, San 31 Hyoja-dong, Nam-gu, Pohang-si, Gyungbuk, 790-784, Republic of Korea*

Abstract

We have measured extremely large coercive magnetic fields of up to 55 T in $\text{Sr}_3\text{NiIrO}_6$, with a switched magnetic moment $\approx 0.8 \mu_{\text{B}}$ per formula unit. As far as we are aware, this is the largest coercive field observed thus far. This extraordinarily hard magnetism has a completely different origin from that found in conventional ferromagnets. Instead, it is due to the evolution of a frustrated antiferromagnetic state in the presence of strong magnetocrystalline anisotropy due to the overlap of spatially-extended Ir^{4+} $5d$ orbitals with oxygen $2p$ and Ni^{2+} $3d$ orbitals. This work highlights the unusual physics that can result from combining the extended $5d$ orbitals in Ir^{4+} with the frustrated behaviour of triangular lattice antiferromagnets.

PACS numbers: 71.70.Ej, 75.30.Gw, 75.50.Vv

I. INTRODUCTION

Oxides containing iridium in the Ir^{4+} ($5d^5$) state have received much recent attention because the energy scales for spin-orbit interactions (SOIs), Coulomb repulsion, and crystalline-electric fields are all very similar [1–11]. This unusual situation, in comparison to analogous $3d$ systems, results from a decrease in the strength of correlation effects and an increase in SOIs as one descends the periodic table. Usually, the Coulomb repulsion and SOIs are responsible for Hund’s rules that determine the groundstates of magnetic ions; however, in these $5d$ (and some $4d$) systems, the competition between the three similarly-sized energy scales can result in exotic magnetic states [1–11], leading to proposals for the use of Ir^{4+} -based systems in quantum information processing and other novel applications (see Refs. [2, 9] and references therein). In this paper, we report another manifestation of unusual $5d$ physics: extremely large coercive magnetic fields of up to 55 T in $\text{Sr}_3\text{NiIrO}_6$, with a switched magnetic moment of about $0.8\mu_B$ per formula unit. As far as we are aware, this is the largest coercive field measured thus far, and a factor ~ 5 times those reported recently in novel, ultra-hard ferromagnets [12]. This exemplary hard magnetism is, however, very different from that found in conventional ferromagnets in that it results from an unusual, frustrated, antiferromagnetic ground state that incorporates a relatively large magnetocrystalline anisotropy.

The salient structural details [13] are shown in Fig. 1. The Ni^{2+} and Ir^{4+} magnetic ions in $\text{Sr}_3\text{NiIrO}_6$ occupy oxygen cages that alternate in chains parallel to the c -axis (Fig. 1(a)). These chains are in turn arranged in a hexagonal pattern in the ab -plane (Fig. 1(b)) [13]. The Ni^{2+} is surrounded by a trigonal bipyramid of oxygen atoms, while the Ir^{4+} ion sits in an octahedral oxygen cage. Magnetic frustration is intrinsic to this structure, and can result from antiferromagnetic interactions within the triangular lattice in the ab -plane, and from frustration between nearest-neighbour and next-nearest-neighbour interactions along the c -axis chains. Electronic structure calculations have suggested both possibilities for $\text{Sr}_3\text{NiIrO}_6$ [14–16]; the same calculations indicate that the overlap of spatially-extended Ir^{4+} $5d$ orbitals with oxygen $2p$ and Ni^{2+} $3d$ orbitals leads to a magnetocrystalline anisotropy energy ≈ 13.5 meV. Schematic energy level diagrams for Ir^{4+} and Ni^{2+} are shown in Fig. 1(c); the effective spin of Ni^{2+} is $S = 1$ and that of Ir^{4+} is $S = \frac{1}{2}$ [14–16].

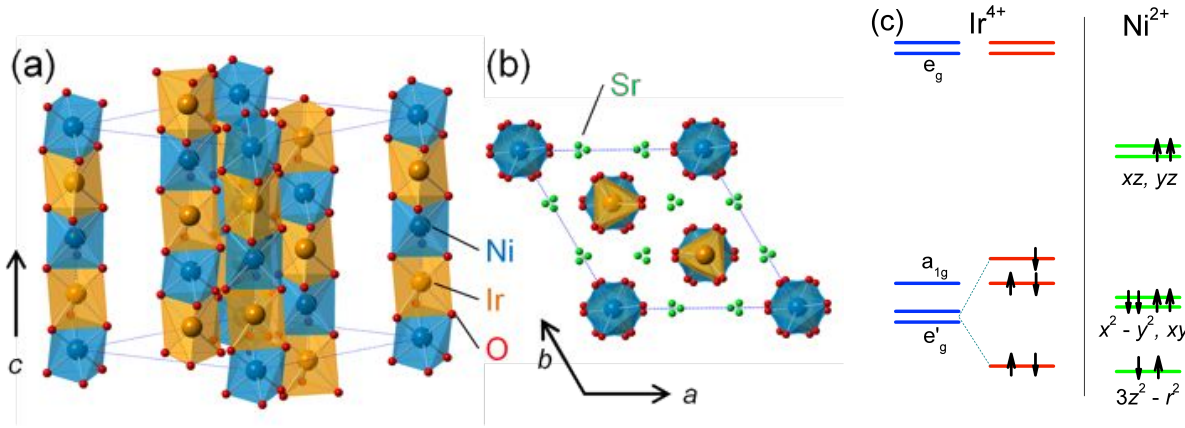


FIG. 1. **Structure and energy levels.** The crystal structure of $\text{Sr}_3\text{NiIrO}_6$ as viewed from the (a) [110] and (b) [001] directions. The Ni^{2+} and Ir^{4+} ions are within oxygen trigonal bipyramids (blue) and oxygen octahedra (orange), respectively. For clarity, Sr ions are not shown in (a). (c) Schematic level diagrams for Ir^{4+} and Ni^{2+} (based on Refs [14–16]). Unperturbed Ir^{4+} levels are shown in blue; a combination of antiferromagnetic interactions and spin-orbit coupling splits the e'_g doublet to give the configuration shown in red. Electron spins are shown as arrows: the effective spin of Ni^{2+} is $S = 1$ and that of Ir^{4+} is $S = \frac{1}{2}$ in the opposite direction.

II. RESULTS

A. Low-field magnetization and dynamics

Our study involves 10 different samples of $\text{Sr}_3\text{NiIrO}_6$ from several different batches encompassing minor variations in growth conditions. The results for all samples are rather consistent; typical data from four single crystals (labelled S1 to S4) and three polycrystalline samples (P1, P2, P3) are shown in the figures that follow. Note that sample S2 is a very small crystal with exceptionally clean hexagonal faces containing virtually no visible defects; as will be seen below, this apparent cleanliness is of relevance to the timescales over which the remanent magnetization persists.

Typical examples of low-magnetic-field DC magnetization data for $\text{Sr}_3\text{NiIrO}_6$ (samples S1, S2 and P1) are shown in Fig. 2. Magnetic order sets in below 85 K, being marked by a broad feature in magnetization (M) vs. temperature (T) data (Fig. 2(a)), and additional peaks in elastic neutron scattering [17–19]. The neutron diffraction data are consistent with either

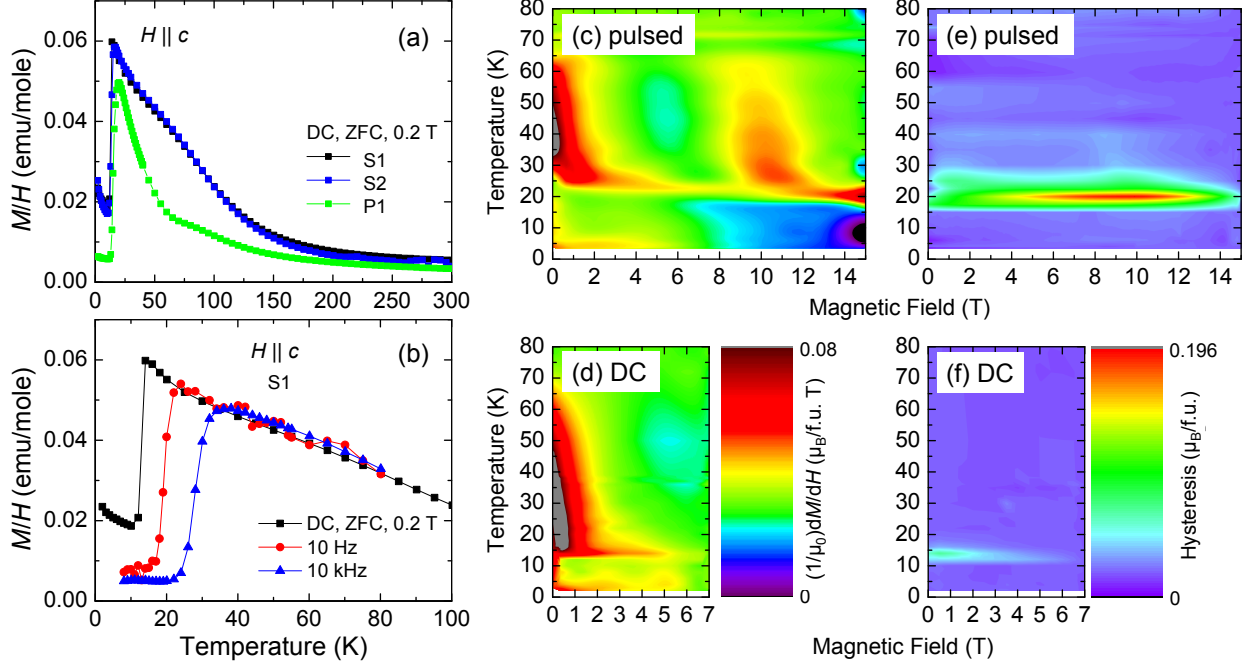


FIG. 2. **Frustration-induced slow dynamics.** (a) DC magnetic susceptibility ($\chi = M/H$) as a function of temperature T for $\text{Sr}_3\text{NiIrO}_6$ single-crystal samples S1 and S2 and polycrystalline sample P1. The onset of magnetic order is marked by a broad hump superimposed on the background slope and centered on $T \approx 85$ K. (b) T -dependent χ data for $\text{Sr}_3\text{NiIrO}_6$ single crystal sample S1 measured DC (black) and using an AC susceptometer operated at frequencies of 10 Hz (red) and 10 kHz (blue). The sharp fall in χ shifts to higher T as the frequency increases. The contour plots show dM/dH versus $\mu_0 H$ and T for polycrystalline sample P2 measured (c) in a pulsed magnetic field with a sweep rate ≈ 3500 T/s and (d) in a SQUID (DC) magnetometer with a magnetic field sweep rate of 0.008 T/s. Corresponding plots of the hysteresis between falling and rising magnetic field sweeps, defined as $\text{hysteresis} = [M(H, T)_{\text{falling}} - M(H, T)_{\text{rising}}]$, are shown in (e) (pulsed field) and (f) (SQUID). Note that as the field sweep rate increases, features in dM/dH and regions of pronounced hysteresis are pushed to higher T .

a partially-disordered antiferromagnet [20] or an amplitude-modulated antiferromagnetic state at low T . Despite the onset of long-range order at 85 K, the heat capacity is nearly featureless between 4 and 250 K [18].

Fig. 2(b) shows the DC magnetic susceptibility of $\text{Sr}_3\text{NiIrO}_6$ single crystal sample S1, in an applied field of $\mu_0 H = 0.2$ T, and the AC susceptibility for an oscillating field amplitude of 10^{-3} T at 10 Hz and 10 kHz. In all three data sets, the sharp drop in M already seen in

Fig. 2(a) is observed as T is lowered. However, the temperature at which the drop occurs is frequency dependent; the half-height point occurs at 28 K for 10 kHz, 20 K for 10 Hz, and 13 K for DC measurements. Further evidence of slow dynamics over a similar temperature range is seen in the contour plot in Figs. 2 (c) to (f). Here we show $dM(H, T)/dH$ on the initial field upswing following zero-field cooling for polycrystalline sample P2. These data were measured in a 7 T SQUID magnetometer with a field-sweep rate ≈ 0.008 T/s (Fig. 2(d)) and in a pulsed magnetic field with a sweep rate ≈ 3500 T/s (Fig. 2(c)), where the pulse shape is shown in Fig. 6(a). Corresponding plots of the hysteresis in M between rising and falling magnetic field sweeps are shown in (e) (pulsed field) and (f) (SQUID). As the field sweep rate increases (and therefore the timescale of the measurement decreases), features in dM/dH and regions of pronounced hysteresis are pushed to higher T . Thus, this dependence of M on sweep rate is analogous to the frequency dependence seen in the AC susceptibility data (Fig. 2(b)), where decreasing the measurement timescale forces features in M to higher T . Similar phenomena have been seen in previous experiments within the ordered phase; as T was lowered below 30 K, a frequency-dependent crossover occurred to hysteretic magnetic behaviour as a function of T and H , as well as a strong frequency dependence of the AC susceptibility [17–19]. A number of other frustrated antiferromagnets isostructural with $\text{Sr}_3\text{NiIrO}_6$ show qualitatively similar frequency-dependent magnetic behaviour [21–33].

B. Large coercive fields

Large coercive fields are demonstrated in Fig. 3, which shows pulsed-field $M(H)$ data for four representative samples of $\text{Sr}_3\text{NiIrO}_6$ (the field-pulse profile is shown in Fig. 6(a)). Data for Figs. 3(a), (b), and (d) are calibrated against absolute measurements on the same samples in quasistatic magnetic fields of up to 13 T.

Though the behaviour of all samples is similar, showing that the large coercive fields are intrinsic to $\text{Sr}_3\text{NiIrO}_6$, there are some detail differences from sample to sample. In Fig. 3(a) (single crystal S3), the magnetic hysteresis for $\mathbf{H} \parallel \mathbf{c}$ is superimposed on a linear $M(H)$ background, and shows a large $\mu_0 H_c = 34.1$ T and a remanent moment of $0.45\mu_B$ per formula unit at zero field. The magnetization jump at 34.1 T is $\approx 0.8\mu_B$ per formula unit. The data in Fig. 3(e) (Sample S4) show an even larger $\mu_0 H_c = 42.7$ T. As mentioned above, sample S2 is a very small single crystal with exceptionally clean faces, and Fig. 3(c)) shows

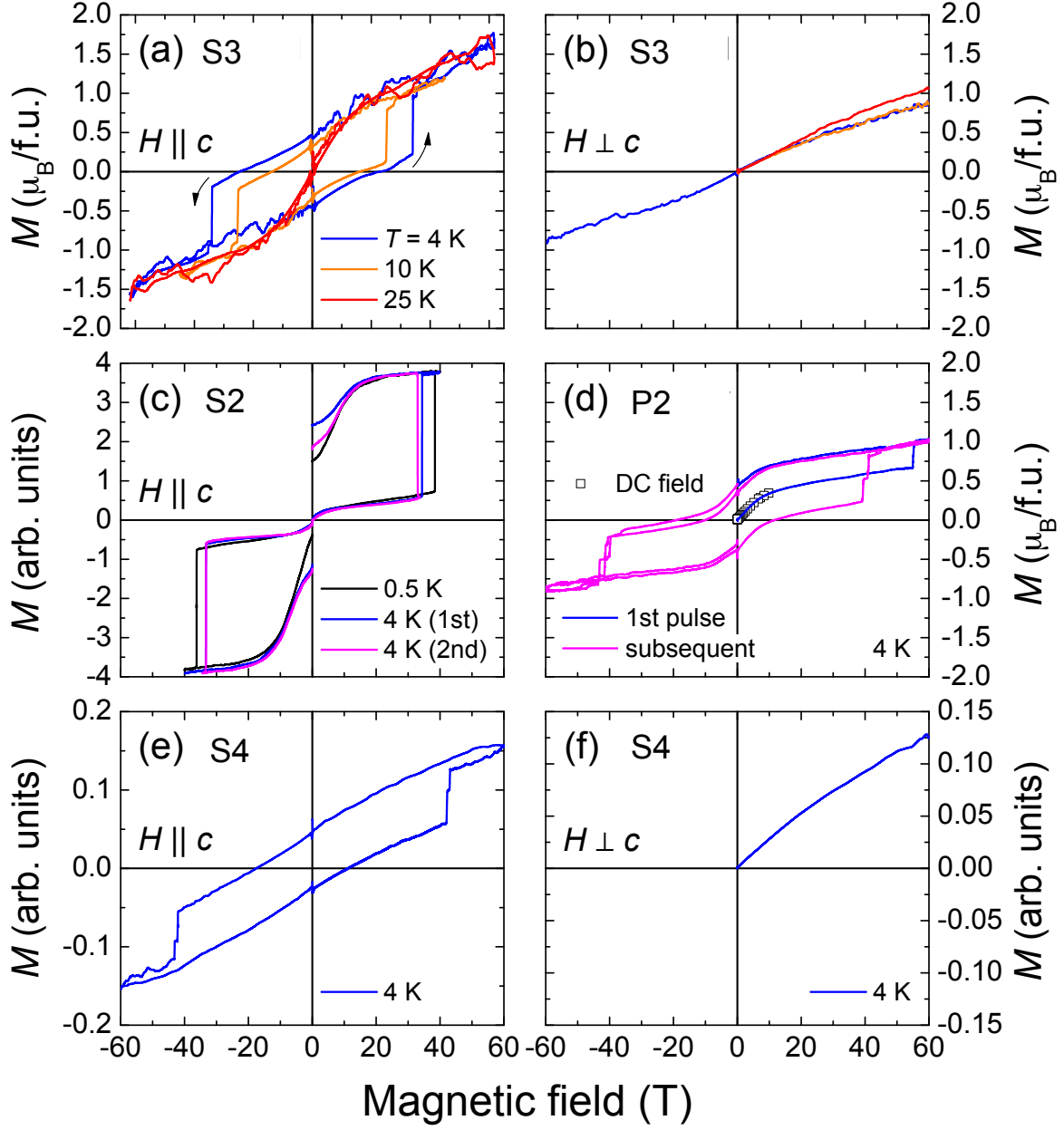


FIG. 3. **Hysteresis loops and large coercive fields.** Magnetization M as a function of magnetic field $\mu_0 H$ measured in a series of pulses using a capacitor-bank-driven 65 T pulsed magnet. Sample numbers, field directions and measurement temperatures T are given in each section of the figure; the vertical jumps in M occur at the coercive field, $\mu_0 H_c$. In (b), (f) no hysteresis is observed in the $\mathbf{H} \perp \mathbf{c}$ configurations. In (a), (b), and (d), absolute magnetization values, measured in commercial SQUID and vibrating-sample magnetometers, were used to calibrate the pulsed field data.

that it exhibits qualitatively different behaviour: the coercive field is very large (38.4 T), as in other samples, but M relaxes during the millisecond timescales (see Fig. 6(a)) of the downsweep of the magnetic field. All subsequent field pulses after the first one show jumps of similar height, consistent with relaxation of M back to zero between field pulses. On the other hand, in Fig. 3(a), (b), (d), (e), and (f) the first upsweeps following a zero-field cool result in an M jump about half the height of subsequent jumps, showing that the latter represent a complete reversal of M . For those samples, two consecutive magnetic fields sweeps in the same direction produce no jump (not shown). In polycrystalline sample P2 (Fig. 3(d)), the $M(H)$ data also show some curvature at low fields, but M does not relax back to zero between field pulses. (As will be shown in Fig. 4(a) below, polycrystalline sample P3 shows similar behaviour, but superimposed on a much less curved background.) In the initial up-sweep, M jumps at a record-high magnetic coercive field of $\mu_0 H_c = 55$ T after zero-field cooling; in subsequent pulses, the M jump doubles in height, but is observed at lower fields (40 T). Note that all samples exhibit a higher H_c value in the initial field sweep after zero-field cooling, compared to those seen in subsequent field sweeps; we shall return to this behaviour below. Finally, we remark that the jumps in M are sharp, occurring over a small range of field (< 1 T at 4 K). In particular, the transition width in Fig. 3(c) is $\lesssim 0.03$ T.

There is no systematic dependence of the magnetic hysteresis on details of the growth method in the samples shown in Fig. 3 or in the three other samples measured, suggesting that all samples have the same Ni/Ir ratio. There does, however, appear to be a pinning effect that stabilizes M in most of the samples; in such cases, the remanent magnetization was found to persist unchanged for at least 24 hours at $T = 4$ K. By contrast, sample S2 in Fig. 3(c) shows magnetic relaxation on millisecond timescales (*i.e.* similar timescales to the downsweep of the pulsed field; see Fig. 6(a)). In addition, none of the samples studied appear to show signs of saturation of the magnetization even in fields of 65 T. The anisotropy of the hysteresis is illustrated in Figs. 3(b) and (f); here $M(H)$ of single crystals S3 and S4 is shown for $\mathbf{H} \perp \mathbf{c}$. For this field direction, no jump in M or hysteresis is observed. In both single crystals, M is comparable in size at 65 T for $\mathbf{H} \perp \mathbf{c}$ and $\mathbf{H} \parallel \mathbf{c}$.

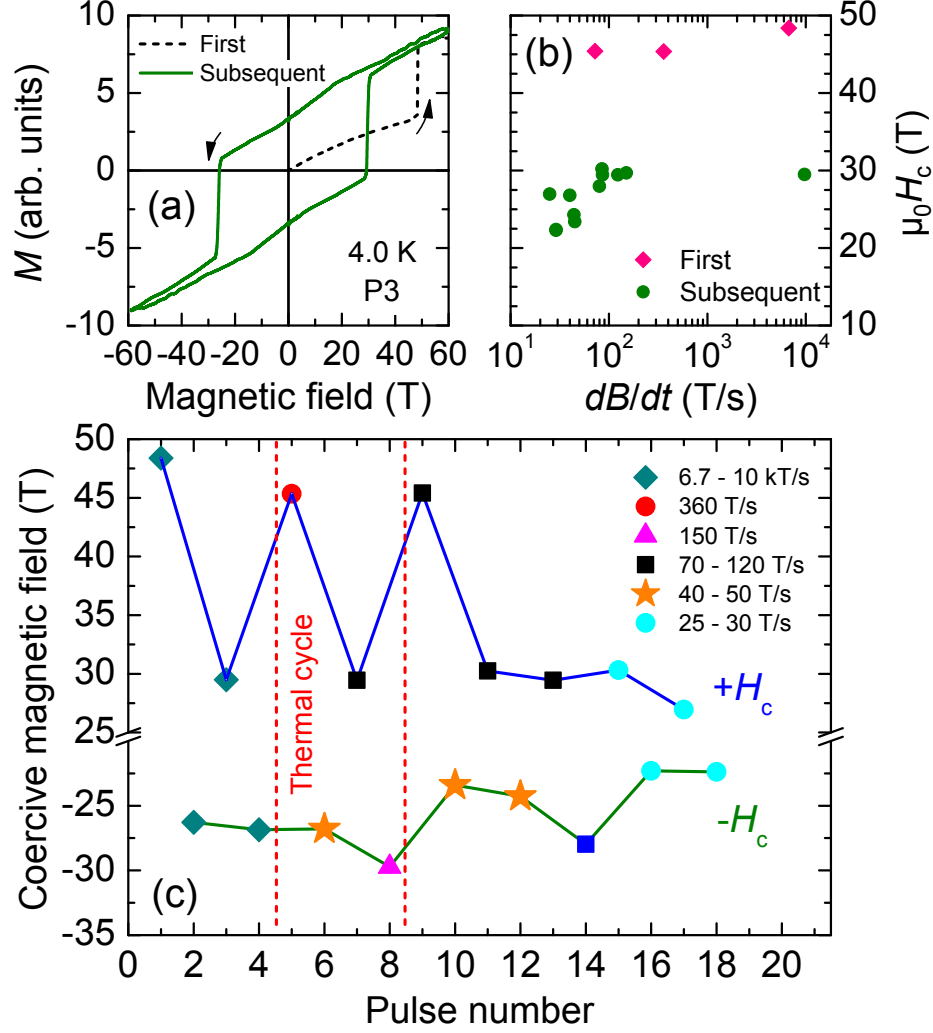


FIG. 4. **Sweep-rate dependence of the coercive field.** (a) $M(H)$ data for polycrystalline sample P3 measured in a capacitor bank-driven pulsed magnet. Black dotted lines denote the initial pulse after zero-field cooling whilst the green solid line indicates data for subsequent pulses at 4 K. (b) Sweep-rate dependence of coercive magnetic field ($\mu_0 H_c$). (c) History dependence of coercive magnetic field ($\mu_0 H_c$) under various sweep rates (plotted as a function of pulse number). For sweep rates larger than 360 T/s, a capacitor-bank-driven pulsed magnet was used; other data were taken using the generator-driven 60 T Long-Pulse Magnet (see Fig. 6 for magnetic field profiles). Twice during this experiment, the sample was warmed to room temperature (denoted by red vertical dashed lines).

C. Dynamics, and history- and temperature dependences of the coercive field

In view of the field-sweep-rate dependence of the low-field magnetization noted earlier (Fig. 2(b)-(f)), it is interesting to see if the hysteresis loops are affected by similar dynamical issues, and so Fig. 4 features $M(H)$ measurements of polycrystalline sample P3 in the Los Alamos generator-driven 60 T Long-Pulse Magnet, which provides sweep rates between 25 and 360 T/s, and in a capacitor-driven 65 T magnet with faster sweep rates (pulse shapes are shown in Fig. 6). Fig. 4(a) once again demonstrates that the coercive field is higher on the initial field sweep after zero-field cooling (c.f. Figs. 3(c) and (d)), whilst (b) shows that this trend also occurs at lower field-sweep rates. The history dependence of the coercive field throughout a sequence of field pulses of varying sweep rate and a couple of thermal cycles to room temperature and back is illustrated in Fig. 4(c). All of these data show that the magnetic hysteresis loop is robust at least down to 25 T/s and illustrate that on magnet pulses subsequent to the initial pulse following zero-field cooling, H_c is slightly smaller in lower field sweep rates; this was observed in all measured samples.

The T -dependences of $M(H)$ for $\mathbf{H} \parallel \mathbf{c}$ and $\mathbf{H} \perp \mathbf{c}$ are shown in Figs. 3(a) and (b) for single crystal S3. For $\mathbf{H} \perp \mathbf{c}$, M for $T < 25$ K is suppressed compared to the value at 25 K, consistent with antiferromagnetic exchange interactions [36]. For $\mathbf{H} \parallel \mathbf{c}$, hysteresis is observed at 10 K but has disappeared by 25 K. The T -dependence of H_c is given in more detail in Fig. 5(a), which shows dM/dH data for $\mathbf{H} \parallel \mathbf{c}$ (sample S2); peaks occur at the coercive field, H_c . Fig. 5(b) shows that H_c decreases linearly with increasing T (data from samples S2 and S3), extrapolating to zero at ≈ 25 K. This is close to the onset of hysteretic behaviour and the frequency-dependent fall in M (see Fig. 2(b-f)), linking the observation of finite coercive field with the low-temperature phase of the antiferromagnetic groundstate. The almost identical variations of H_c with temperature in the two samples show that the value of this field and its temperature dependence are intrinsic to $\text{Sr}_3\text{NiIrO}_6$ single crystals, whereas the persistence (or not) of the remanent magnetization depends on extrinsic factors such as defects or disorder (the same samples are used in Figs. 3(a),(c)).

Finally, we note that a coercive field $\mu_0 H_c \approx 22$ T was measured using polycrystalline samples of $\text{Sr}_3\text{NiIrO}_6$ in Ref. [17]. All of our polycrystalline samples exhibit low-temperature coercive fields $\mu_0 H_c \approx 40$ T, very similar to those seen in the single crystals (see Figs. 3 and 4). Therefore, the difference between polycrystalline and single-crystal samples cannot

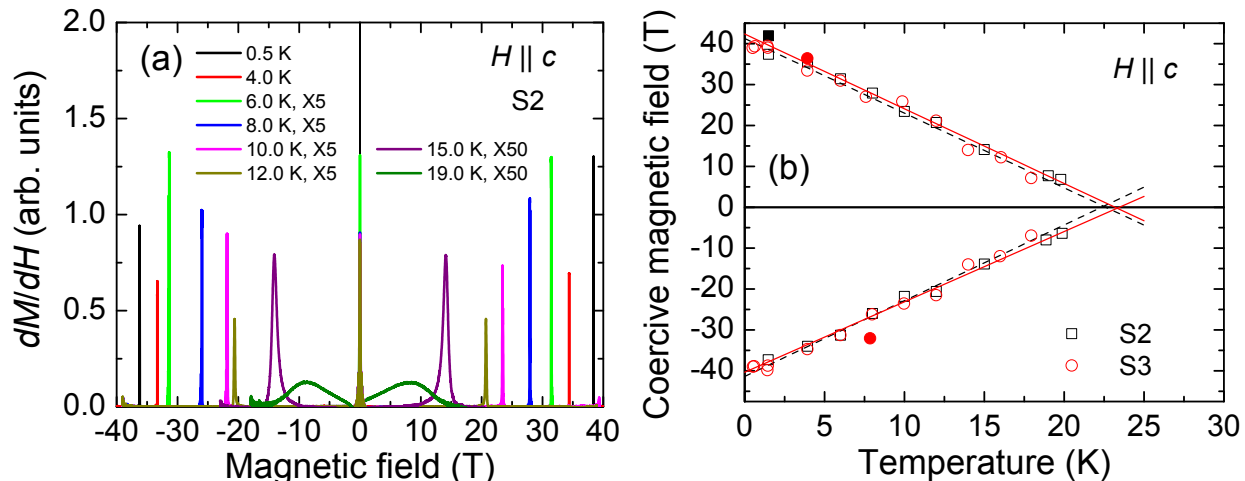


FIG. 5. **Delineating the region of large coercive field.** (a) dM/dH for single-crystal sample S2 at several T for $\mathbf{H} \parallel \mathbf{c}$ (c.f. Fig. 3(a,c)). The peaks denote the sharp change in M at the coercive field; note that multiplication factors of 5 and 50 are applied for 6, 8, 10 K and 15, 19 K data, respectively as the peak broadens with increasing T . (b) T -dependence of the coercive field for single crystals S2 and S3. Filled symbols indicate the result taken in the initial pulse after zero-field cooling from room T ; these show slightly larger H_c values compared those measured in subsequent pulses (see Fig. 4). Lines are linear fits to the data.

account for the much lower values of H_c observed in Ref. [17] compared to those in this work.

III. DISCUSSION

A. Summary of results

Combining the H - and T -dependent magnetization studies of $\text{Sr}_3\text{NiIrO}_6$, a picture emerges of an antiferromagnetic order [19] for $T \lesssim 30$ K and $H = 0$ that evolves in applied magnetic fields. This evolution is manifested most markedly in the sharp jump in magnetization that occurs on rising fields. The field position $\mu_0 H_c$ of the jump shows a similar history and field-sweep-rate dependence for all samples (Figs. 3, 4, 5), with slightly smaller values of H_c occurring at lower sweep rates. This strongly suggests that the magnetization jump at H_c is an intrinsic property of $\text{Sr}_3\text{NiIrO}_6$, with the sweep-rate dependence being caused by sluggish kinetics associated with the magnetic frustration intrinsic to this

structural family [11]; the same frustration is responsible for the slow magnetic relaxation (Figs. 2(c-f)) and the strong variation (13–28 K) of the fall in M with frequency (Fig. 2(b)). By contrast, in systems such as (Sm,Sr)MnO₃ [34], where the magnetization jumps are not intrinsic, but associated with quenched disorder, the smaller the field-sweep rate, the *larger* the field needed to realize the transition, the opposite of what we observe in Sr₃NiIrO₆ (Fig. 4).

It is likely that the millisecond-timescale magnetic relaxation observed in the hysteresis loops for sample S2 (Fig. 3(c)) is also intrinsic behaviour due to frustration, whilst samples S3, S4, P2 (Figs. 3(a), (d), (e)) and P3 (Fig. 4(a)) and all other samples studied exhibit pinning or freezing of the magnetization or an order-by-disorder mechanism, as seen at lower fields in isostructural Ca₃CoMnO₆ [35]. In the latter mechanism, magnetic-site disorder disrupts longer-range interactions, leading to a reduction of frustration [35].

B. Comparison with ferromagnets and other systems

Magnets with high coercivity, *i.e.*, “hard” magnets, are important for a wide range of applications involving magnetic actuation and induction, such as loud speakers, wind turbines and electric motors [36]. In rare-earth iron boride magnets, among the hardest commercial magnets, $\mu_0 H_c$ can be as large as 1.5 T at room temperature [37]. At cryogenic temperatures, magnetic hysteresis effects can extend to higher fields, *e.g.*, up to 10 T in the colossal magnetoresistance manganites, and in Li₂(Li_{1-x}Fe_x)N, Gd₅Ge₄, Ga-doped CeFe₂, LuFe₂O₄, and Fe_{1/4}TaSe₂ [12, 28, 38–42]. Large coercive fields in such magnets are typically caused by magnetocrystalline anisotropy due to SOI [37], whilst magnetic hysteresis results from a combination of domain dynamics and anisotropy [36]. In traditional ferromagnets, domains result from competition between the short-range exchange interactions that prefer parallel spin alignment, and the free-energy penalty of maintaining a magnetic field in an extended region of space around the sample [36]. The effect of this competition is that the energy scale for switching magnetic domains can be orders of magnitude smaller than those of the nearest-neighbor ferromagnetic exchange interactions. Generally, the microscopic order in a traditional ferromagnet does not change significantly around the hysteresis loop as the domains change direction and/or the domain walls move [36].

By contrast, the conventional phenomenology of ferromagnetic domains is *not* involved

in the notable H_c values observed for $\text{Sr}_3\text{NiIrO}_3$ (35 – 55 T, this work) and in the lower, but nevertheless impressive, values measured in the isostructural family of frustrated triangular-lattice antiferromagnets, $\text{Ca}_3\text{Co}_2\text{O}_6$ (7 T) [28], and $\text{Ca}_3\text{CoMnO}_6$ (10 T) [33, 43], $\text{Sr}_3\text{CoIrO}_6$ (≈ 20 T) [18], and $\text{Ca}_3\text{CoRhO}_6$ (≈ 30 T) [23]. $\text{Sr}_3\text{NiIrO}_6$ is initially antiferromagnetic after zero-field cooling and its magnetic groundstate must evolve to produce a net magnetization [19]. The energy scale for the coercive field ($\mu_0 H_c = 34 - 55$ T) is roughly of the same order of magnitude as the temperature of the onset of magnetic hysteresis (13 – 28 K), and long-range order (85 K), consistent with evolution of the magnetic order driven by large magnetic fields. Indeed, in compounds isostructural with $\text{Sr}_3\text{NiIrO}_6$, the microscopic order has been shown to change around the hysteresis loop using elastic neutron diffraction measurements [43, 44]. We can therefore infer that the magnetic hysteresis in $\text{Sr}_3\text{NiIrO}_6$ can be attributed to the evolution of a microscopic frustrated order with magnetic field, rather than domain effects (*c.f.* Ref. [45]).

As mentioned previously, electronic structure calculations suggest that the magnetocrystalline anisotropy in $\text{Sr}_3\text{NiIrO}_6$ results from the configuration of overlapping orbitals in Ir^{4+} -O- Ni^{2+} chain [14–16]. This picture is supported by the prevalence of relatively large coercive magnetic fields in the isostructural family members that have $4d$ or $5d$ ions (with relatively extended orbitals) on the octahedral site and $3d$ ions on the bipyramidal site: $\text{Ca}_3\text{CoRhO}_6$, $\text{Sr}_3\text{NiIrO}_6$ and $\text{Sr}_3\text{CoIrO}_6$ [17, 18, 23]. The exceptional coercive magnetic field in the title compound serves as another example of notable physical effects resulting from the unusual $5d$ orbital physics of Ir^{4+} .

IV. CONCLUSION

In conclusion, we observed coercive magnetic fields of 34–55 T for $\mathbf{H} \parallel \mathbf{c}$ in flux-grown single crystals and polycrystalline $\text{Sr}_3\text{NiIrO}_6$, to our knowledge, a record high coercive magnetic field for any material. $\text{Sr}_3\text{NiIrO}_6$ shows signatures of a type of frustrated antiferromagnetic order in zero field [19], and the hysteresis loop is likely due to evolution of this microscopic order. The high coercive magnetic field is consistent with the large magnetocrystalline anisotropy predicted in *ab-initio* calculations for this compound, due to the Ir^{4+} $5d$ orbitals overlapping via intermediate oxygen with Ni^{2+} $3d$ orbitals.

V. METHODS

A. Sample growth

Polycrystalline $\text{Sr}_3\text{NiIrO}_6$ was prepared through solid-state reaction at 1300°C . Single crystals of $\text{Sr}_3\text{NiIrO}_6$ were grown from either a stoichiometric or 20 % Ni-rich or 20 % Ir-rich (in molar ratio) composition using K_2CO_3 as flux. The single crystals are hexagonal plates with typical dimensions $2 \times 2 \times 0.5 \text{ mm}^3$.

B. Magnetization measurements

Quasistatic-field magnetization ($M(H)$) data were measured in a vibrating sample magnetometer in a superconducting magnet (PPMS-14, Quantum Design), or in a SQUID (MPMS-7, Quantum Design). AC susceptibility data were measured in a 7 T AC SQUID and an ac susceptometer in a 14 T PPMS (Quantum Design).

The pulsed-field magnetization experiments used a 1.5 mm bore, 1.5 mm long, 1500-turn compensated-coil susceptometer, constructed from 50 gauge high-purity copper wire [46]. When a sample is within the coil, the signal is $V \propto (dM/dt)$, where t is the time. Numerical integration is used to evaluate M . Samples were mounted within a 1.3 mm diameter ampoule that can be moved in and out of the coil. Accurate values of M are obtained by subtracting empty-coil data from that measured under identical conditions with the sample present. The susceptometer is calibrated by scaling low-field M values to match those recorded with a sample of known mass measured in a commercial SQUID or vibrating-sample magnetometer.

Fields were provided by a 65 T short-pulse magnet energized by a 4 MJ capacitor bank, or the generator-driven 60 T Long-Pulse Magnet at NHMFL Los Alamos; the field versus time profiles for these two magnets are shown in Fig. 6. The susceptometer was placed within a ^3He cryostat providing T s down to 0.4 K. $\mu_0 H$ was measured by integrating the voltage induced in a ten-turn coil calibrated by observing the de Haas-van Alphen oscillations of the belly orbits of the copper coils of the susceptometer [46].

In measuring hysteresis loops, the initial field sweep (up and down) is performed after zero-field cooling from room temperature. Subsequent pulses are delivered after 40 to 60 minutes (the cooling time of the magnet in question) while maintaining constant sample temperature.

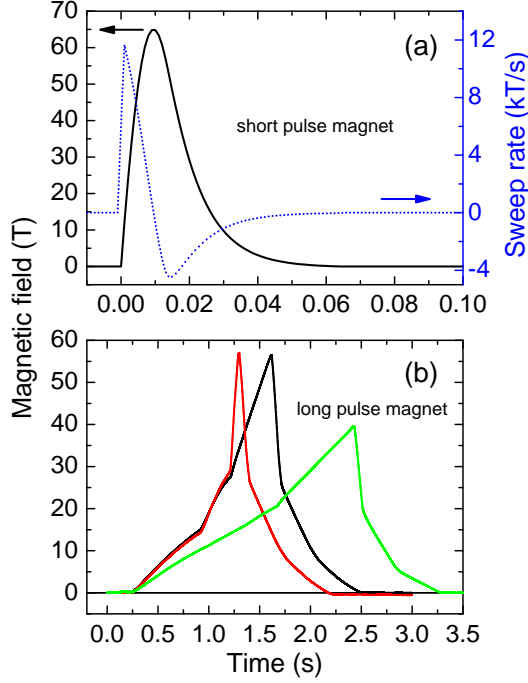


FIG. 6. **Time-dependence of magnetic fields** for (a) a capacitor-bank-driven 65 T short-pulse magnet and (b) three examples of the controlled sweep patterns possible with the generator-driven 60 T Long Pulse Magnet. (a) $\mu_0 dH/dt$ for the short-pulse magnet is shown in blue (right axis). In (b), the three stages in each of the field-sweep patterns are due to three separate coils that are energized in sequence by the generator.

VI. REFERENCES

-
- [1] Kim, B.J., *et al.*. Phase-Sensitive Observation of a Spin-Orbital Mott State in Sr_2IrO_4 . *Science* **323**, 3129 (2009).
 - [2] Lovesy, S.W., Khalyavin, D.D., Manuel, P., Chapon, L.C. & Qi, T.F.. Magnetic symmetries in neutron and resonant x-ray Bragg diffraction of four iridium oxides, *J. Phys.: Condens. Matter* **24**, 496003 (2012).
 - [3] Chapon, L.C., and Lovesy, S.W.. The magnetic motif and the wavefunction of Kramers ions in strontium iridate. *J. Phys.: Condens. Matter* **23**, 252201 (2011)
 - [4] Shitade, Atsuo *et al.*. Quantum Spin Hall Effect in a Transition Metal Oxide Na_2IrO_3 . *Phys.*

- Rev. Lett.* **102**, 256403 (2009)
- [5] Laguna-Marco, M. A. *et al.*. Orbital Magnetism and Spin-Orbit Effects in the Electronic Structure of BaIrO₃. *Phys. Rev. Lett.* **105**, 216407 (2010)
 - [6] Chikara, S., Korneta, O. Crummett, W. P., DeLong, L. E., Schlottmann, P., & Cao, G.. Giant magnetoelectric effect in the $J_{\text{eff}} = 1/2$ Mott insulator Sr₂IrO₄. *Phys. Rev. B* **80**, 140407 (2009)
 - [7] Chaloupka, J., Jackeli, George & Khaliullin, Giniyat. Kitaev-Heisenberg Model on a Honeycomb Lattice: Possible Exotic Phases in Iridium Oxides A₂IrO₃. *Phys. Rev. Lett.* **105**, 027204 (2010)
 - [8] Witczak-Krempa, William and Kim, Yong Baek. Topological and magnetic phases of interacting electrons in the pyrochlore iridates. *Phys. Rev. B* **85**, 045124 (2012)
 - [9] Choi, S.K., *et al.* Spin Waves and Revised Crystal Structure of Honeycomb Iridate Na₂IrO₃. *Phys. Rev. Lett.* **108**, 127204 (2012)
 - [10] Kim, B. J., *et al.*. Novel $J_{\text{eff}} = 1/2$ Mott state induced by relativistic spin-orbit coupling in Sr₂IrO₄, *Phys. Rev. Lett.*, **101** 076402 (2008)
 - [11] Kim, Heung-Sik, Kim, Choong H., Jeong, Hokyun, Jin, Hosub & Yu, Jaejun. Strain-induced topological insulator phase and effective magnetic interactions in Li₂IrO₃. *Phys. Rev. B* **87**, 165117 (2013)
 - [12] Jesche, A., *et al.*. Giant magnetic anisotropy and tunneling of the magnetization in Li₂(Li_{1-x}Fe_x)N. *Nature Communications* **5**, 3333 (2014)
 - [13] Nguyen, T.N., & Zur Loye, H.C.. A family of one-dimensional oxides: Sr₃MIrO₆ (M = Ni, Cu, Zn): Structure and Magnetic Properties. *J. Solid State Chem.* **117** 300 (1995).
 - [14] Zhang, G.R., Zhang, X.L., Jia, T., Zeng, Z. & Lin, H.Q.. Intrachain antiferromagnetic interaction and Mott state induced by spin-orbit coupling in Sr₃NiIrO₆. *J. Appl. Phys.* **107** 09E120 (2010)
 - [15] Sarkar, Soumyajit, Kanungo, Sudipta & Saha-Dasgupta, T.. Ab initio study of low-dimensional quantum spin systems *Sr₃NiPtO₆*, *Sr₃CuPtO₆*, and *Sr₃NiIrO₆* *Phys. Rev. B* **82**, 235122 (2010)
 - [16] Ou, Xuedong, & Wu, Hua. Impact of spin-orbit coupling on the magnetism of Sr₃MIrO₆ (M = Ni, Co). Preprint arXiv:1312.7411
 - [17] Flahaut, D., *et al.*. A magnetic study of the one dimensional Sr₃NiIrO₆ compound *Eur. Phys.*

- J. B* **35**, 317 (2003)
- [18] Mikhailova, D., *et al.* Magnetic properties and crystal structure of $\text{Sr}_3\text{CoIrO}_6$ and $\text{Sr}_3\text{NiIrO}_6$. *Phys. Rev. B* **86** 134409 (2012)
 - [19] Lefrancois, E., *et al.* Magnetic order in the frustrated Ising-like chain compound $\text{Sr}_3\text{NiIrO}_6$. Preprint arXiv: 1403.4815v1
 - [20] Mekata, M.. Antiferro-Ferrimagnetic Transition in Triangular Ising Lattice. *J. Phys. Soc. Jpn.* **42**, 76 (1977)
 - [21] Kageyama, H., Yoshimura, K., & Kosuge, K.. Synthesis and Magnetic Properties of New Series of One-Dimensional Oxides $\text{Ca}_3\text{Co}_{1+x}\text{B}_{1-x}\text{O}_6$ ($B = \text{Ir, Ru}$). *J. Solid State Chem.* **140**, 14 (1998).
 - [22] Kawasaki, S., Takano, M., & Inami, T.. Synthesis, Structure, and Magnetic Properties of Ca_3BMnO_6 ($B = \text{Ni, Zn}$) and $\text{Ca}_3\text{ZnCoO}_6$ Crystallizing in the K_4CdCl_6 Structure. *J. Solid State Chem.* **145**, 302 (1999).
 - [23] Niitaka, S., Yoshimura, K., Kosuge, K., Nishi, M., & Kakurai, K.. High-Field Magnetization and Neutron Diffraction Studies of One-Dimensional Compound $\text{Ca}_3\text{CoRhO}_6$. *Phys. Rev. Lett.* **87**, 177202 (2001).
 - [24] Stitzer, K.E., Henley, W.H., Claridge, J.B., zur Loye, H.-C., & Layland, R.C.. $\text{Sr}_3\text{NiRhO}_6$ and $\text{Sr}_3\text{CuRhO}_6$: Two New One-Dimensional Oxides. Magnetic behaviour as a Function of Structure: Commensurate vs Incommensurate. *J. Solid State Chem.* **164**, 220 (2002).
 - [25] Rayaprol, S., Sengupta, K., & Sampathkumaran, E.V.. Magnetic frustration in the stoichiometric spin-chain compound $\text{Ca}_3\text{CoIrO}_6$. *Phys. Rev. B* **67**, 180404 (2003).
 - [26] Loewenhaupt, M., Schlafer, W., Niazi, A. & Sampathkumaran, E.V.. Evidence for the coexistence of low-dimensional magnetism and long-range order in $\text{Ca}_3\text{CoRhO}_6$. *Europhys. Lett.* **63**, 374 (2003).
 - [27] Hardy, V., *et al.* Specific heat investigation of the magnetic ordering in two frustrated spin-chain oxides: $\text{Ca}_3\text{Co}_2\text{O}_6$ and $\text{Ca}_3\text{CoRhO}_6$. *J. Phys.: Cond. Matter* **15**, 5737 (2003).
 - [28] Hardy, V., Flahaut, D., Lees, M.R., & Petrenko, O.A.. Magnetic quantum tunneling in $\text{Ca}_3\text{Co}_2\text{O}_6$ studied by ac susceptibility: Temperature and magnetic-field dependence of the spin-relaxation time. *Phys. Rev. B* **70**, 214439 (2004).
 - [29] Mohapatra, N., Iyer, K.K., Rayaprol, S., & Sampathkumaran, E.V.. Geometrically frustrated magnetic behaviour of $\text{Sr}_3\text{NiRhO}_6$ and $\text{Sr}_3\text{NiPtO}_6$. *Phys. Rev. B* **75**, 214422 (2007).

- [30] Choi, Y.J., Yi, H.T., Lee, S., Huang, Q., Kiryukhin, V., & Cheong, S.-W.. Ferroelectricity in an Ising Chain Magnet. *Phys. Rev. Lett.* **100**, 047601 (2008).
- [31] Agrestini, S., Mazzoli, C., Bombardi, A., & Lees, M.R.. Incommensurate magnetic ground state revealed by resonant x-ray scattering in the frustrated spin system $\text{Ca}_3\text{Co}_2\text{O}_6$. *Phys. Rev. B* **77**, 140403 (2008).
- [32] Agrestini, S., *et al.*. Slow Magnetic Order-Order Transition in the Spin Chain Antiferromagnet $\text{Ca}_3\text{Co}_2\text{O}_6$. *Phys. Rev. Lett.* **106**, 197204 (2011).
- [33] Kim, J.W., *et al.*. Multiferroicity with coexisting isotropic and anisotropic spins in $\text{Ca}_3\text{Co}_{2-x}\text{Mn}_x\text{O}_6$. *Phys. Rev. B* **89**, 060404 (2014).
- [34] Fisher, L.M., *et al.*. Quenched-disorder-induced magnetization jumps in $(\text{Sm},\text{Sr})\text{MnO}_3$. *Phys. Rev. B* **70**, 212411 (2004).
- [35] Kiryukhin, V., *et al.*. Order by Static Disorder in the Ising Chain Magnet $\text{Ca}_3\text{Co}_{2-x}\text{Mn}_x\text{O}_6$. *Phys. Rev. Lett.* **102**, 187202 (2009)
- [36] Cullity B.D., & Graham, C.D.. Introduction to Magnetic Materials. 2nd edition (Wiley, New York, 2009)
- [37] Coey, J.M.D.. Advances in Magnetism - Hard Magnetic Materials: A Perspective. *IEEE Trans. Magn.* **47**, 4671 (2011).
- [38] Autret, C., *et al.*. Magnetization steps in a noncharge-ordered manganite, $\text{Pr}_{0.5}\text{Ba}_{0.5}\text{MnO}_3$. *Appl. Phys. Lett.* **82**, 4746 (2003)
- [39] Morosan, E., *et al.*. Sharp switching of the magnetization in Fe_4TaS_2 . *Phys. Rev. B* **75**, 104401 (2007)
- [40] Haldar, Arabinda, Suresh, K. G., & Nigam, A. K.. Magnetism in gallium-doped CeFe_2 : Martensitic scenario. *Phys. Rev. B* **78** 144429 (2008)
- [41] Wu, Weida, *et al.*. Formation of Pancakelike Ising Domains and Giant Magnetic Coercivity in Ferrimagnetic LuFe_2 . *Phys. Rev. Lett.* **101**, 137203 (2008).
- [42] Ko, K.-T., *et al.*. RKKY Ferromagnetism with Ising-Like Spin States in Intercalated Fe_4TaS_2 . *Phys. Rev. Lett.* **107**, 247201 (2011).
- [43] Jo, Y.J., *et al.*. 3:1 magnetization plateau and suppression of ferroelectric polarization in an Ising chain multiferroic. *Phys. Rev. B* **79**, 012407 (2009)
- [44] Fleck, C.L., Lees, M.R., Agrestini, S., McIntyre, G.J., & Petrenko, O.A.. Field-driven magnetisation steps in $\text{Ca}_3\text{Co}_2\text{O}_6$: A single-crystal neutron-diffraction study. *Europhys. Lett.* **90**,

67006 (2010).

- [45] Yanez-Vilar, S., *et al.* Multiferroic behavior in the double perovskite $\text{Lu}_2\text{MnCoO}_6$. *Phys. Rev. B* **84**, 134427 (2011).
- [46] Goddard, P.A., *et al.* Experimentally determining the exchange parameters of quasi-two-dimensional Heisenberg magnets. *New. J. Phys.* **10**, 083025 (2008).

VII. ACKNOWLEDGMENTS

This work is funded by the U.S. Department of Energy, Basic Energy Sciences program “Science at 100 Tesla”. The NHMFL Pulsed Field Facility is funded by the US National Science Foundation through Cooperative Grant No. DMR-1157490, the State of Florida, and the US Department of Energy. Work in the UK is supported by the EPSRC. PAG and JS would like to thank the University of Oxford for the provision of visiting fellowships. The work at Rutgers was supported by the NSF under Grant number NSF-DMREF-1233349, and the work at Postech was supported by the Max Planck POSTECH/KOREA Research Initiative Program (Grant number 2011-031558) through NRF of Korea funded by MEST.

VIII. AUTHOR CONTRIBUTIONS

J.S., J-W.K. and C.T. carried out the pulsed-field magnetization measurements, analyzed the data and prepared the figures in this paper. C.T., P.A.G. and J.S. constructed the pulsed-field magnetometer. E.D.M. assisted with pulsed-field experiments. The SQUID and AC and DC magnetometry data in this paper were measured by S.G., P.A.G. and A.H.. Samples were grown, characterized and prepared by X.L, Y.S.O. and S-W.C.. The text was written by J.S. and V.Z. with input from all authors. This study is part of a research program on multiferroics directed by V.Z..

IX. ADDITIONAL INFORMATION

The authors declare no competing financial interests.